Journal of Materials Chemistry A

Polyoxometalates as Bifunctional Templates: Engineering Metal Oxides with Mesopores and Reactive Surface for Catalysis

Journal:	*Journal of Materials Chemistry A*
Manuscript ID	TA-ART-09-2019-009614.R1
Article Type:	Paper
Date Submitted by the Author:	27-Oct-2019
Complete List of Authors:	Leng, yan; University of Tennessee Liu, Jixing; University of Tennessee Zhang, Zihao; University of Tennessee Chen, Hao; University of Tennessee Zhang, Pengfei; Shanghai Jiao Tong University, Department of Chemical Engineering; Oak Ridge National Laboratory, Dai, Sheng; Oak Ridge National Laboratory,

Journal Name

ARTICLE

Polyoxometalates as Bifunctional Templates: Engineering Metal Oxides with Mesopores and Reactive Surface for Catalysis

Received 00th January 20xx,
Accepted 00th January 20xx

DOI: 10.1039/x0xx00000x

www.rsc.org/

Yan Leng,[a,b] Jixing Liu,[b] Zihao Zhang,[b] Hao Chen,[b] Pengfei Zhang,[c]* and Sheng Dai[b,d]*

Abstract: Mesoporous metal oxides with optimized porosity and active surface usually exhibit unexpected performance in many applications. However, sacrificial templates and complicated processes are generally required to direct mesopores. Herein, we discover the bifunctional templating talent of polyoxometalate (POM) for generating not only mesopores but also reactive surface into metal oxides, and a facile, recyclable, and general method is reported. By mechanochemically ion-sharing between metal salts and POM, metal precursors undergo pyrolysis around large POM clusters, which can incorporate abundant mesopores into metal oxides (e.g.,Co_3O_4, Fe_3O_4, NiO, La_2O_3, MnO_2, CeO_2, ZrO_2, CuO) with ultrahigh specific surface areas (up to 210 m^2/g) after simply recycled by water washing. Unexpectedly, the oxidative feature of POM naturally contributes to the formation of high valence metal cations on material surface. As an example, the Co_3O_4 sample with both mesopores and enriched surface Co^{3+} species was more active than Co_3O_4 derived from silica template (T_{100}=200°C) and commercial Co_3O_4 (T_{100}=250°C), in CO oxidation. The current strategy may provide a promising route for the commercialization of mesoporous metal oxides with preferred surface features.

Introduction

Metal oxides are very important classes of materials with favorable features of low–cost, rich reserves, redox ability, good stability and so on, which have shown broad applications in heterogeneous catalysis, energy storage and conversion, sensors, and biomedical fields.[1-3] Actually, metal oxides' functional performance significantly depends on their morphology, composition, and crystal structure.[4,5] Being a key factor, embedding porosity into metal oxides can maximally expose active surfaces and accelerate mass transfer,[6,7] and tuning their surface species may induce a highly active facet exposure.[8,9] In this regard, considerable efforts have been devoted to design metal oxides with preferred porosity and surface species.

In general, mesoporous metal oxides have been fabricated through template-assisted processes, which proceed via either soft– or hard–templating methods.[10-13] Soft–templating method typically relies on the self-assembly between metal precursors and block copolymers (e.g., F127, P123, and P108), followed by calcination to crystallize metal oxides and remove organic templates at the same time.[14-16] This method usually needs several days for intermediates aging (solvent evaporation) and the range of mesoporous metal oxides that can be synthesized is limited. For the hard-templating procedure, rigid materials (e.g., porous silica or carbon) are used as the templates with the introduction of metal oxide precursors via impregnation or coprecipitation processes, followed by calcination in air for crystallization, and the removal of silica template in basic solution.[17-22] This procedure termed as "nanocasting" is a more general strategy to obtain a wide range of metal oxides with rich porosity and diverse morphology. For example, Wang et al. utilized a solvent-free chemical method to prepare Co_3O_4–octahedrons, –plates, and –rods, and found that the Co_3O_4–rod exhibited the highest catalytic activity for carbon monoxide (CO) oxidation.[23] Although some important progress has been made to prepare porous metal oxides with better performance, sacrificial templates and complicated processes are generally required by the-state-of-art methods, which somewhat restricted practical application of such metal oxides.

[a] The Key Laboratory of Synthetic and Biological Colloids, Ministry of Education, School of Chemical and Material Engineering, Jiangnan University, Wuxi 214122, Jiangsu, China.
[b] Department of Chemistry, University of Tennessee, Knoxville, TN 37996, USA.
[c] School of Chemistry and Chemical Engineering, Shanghai Jiao Tong University, Shanghai 200240, P. R. China. E-mail: chemistryzpf@sjtu.edu.cn.
[d] Chemical Sciences Division, Oak Ridge National Laboratory Knoxville, TN 37831, USA. E-mail: dais@ornl.gov.
† Electronic Supplementary Information (ESI) available: [details of any supplementary information available should be included here]. See DOI: 10.1039/x0xx00000x

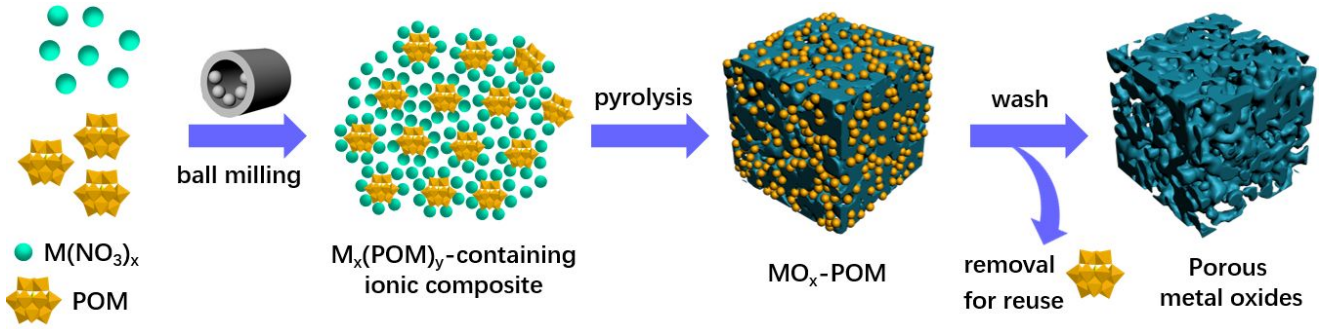

Figure 1. POM-templating mechanochemical route for the synthesis of mesoporous metal oxides.

Polyoxometalates (POMs) are transition metal oxygen clusters with many attractive properties, and have been used extensively as efficient catalysts and building blocks for functional materials.[24-26] Inspired by their unique features, such as large cluster size, rigid backbone, high thermal stability, accessible ion-exchange ability and good solubility in water, we are wondering whether POMs can serve as recyclable anion clusters to support the formation of mesoporous materials. Herein, we present the mechanochemical fabrication of mesoporous metal oxides using a POM–templating ion-sharing strategy, during which POM is a non–sacrificial template that can be easily recovered and reused. Through which, a series of mesoporous metal oxides with high surface areas, including Co_3O_4, Fe_3O_4, CuO, La_2O_3, MnO_2, CeO_2, ZrO_2, and NiO were successfully synthesized. The as–prepared mesoporous $Co_3O_{4(PMo)}$ exhibited excellent catalytic activity in CO oxidation. Investigations on the correlation between Co_3O_4 structure and activity demonstrated that predominantly exposed {110} facets with rich active Co^{3+} sites and low–temperature reducibility may be responsible for the excellent catalytic performance of $Co_3O_{4(PMo)}$.

Experimental section

Characterization

Please see the Supporting Information.

Synthesis of porous metal oxides

2 g of metallic nitrate ($Co(NO_3)_2$, $Ni(NO_3)_2$, $Cu(NO_3)_2$, $Fe(NO_3)_3$, $Zr(NO_3)_4$, $Mn(NO_3)_2$, $La(NO_3)_2$, or $Ce(NO_3)_2$) and 2 g of $Na_3PMo_{12}O_{40}$ or $Na_3PW_{12}O_{40}$ were added into a 25 mL screw–capped stainless–steel reactor along with four stainless steel ball bearings (diameter:1.2 cm). The reactor was placed in a high–speed vibrating ball miller (Retsch MM400), ball milling for 30 min at a vibrational frequency of 30 Hz. The obtained mixture powders were calcinated at 400 °C in air for 2 h with a heating rate of 2 °C min^{-1}. The calcinated black powders were washed with water to remove the most (>70 wt%) of $Na_3PMo_{12}O_{40}$, and was further washed with 0.5 M NaOH to remove the residual $Na_3PMo_{12}O_{40}$. Finally, the solid product was washed with deionized water to remove NaOH and dried overnight at 100 °C. The control sample $Co_3O_{4(Si)}$ was prepared based on the similar procedure using commercial silica (C.A.S. 7631-86-9, Acros organics) as template, which is composed of nonuniform nanospheres and possesses a surface area of ~200 m^2/g. 2 M NaOH solution was used to remove the silica template. Please see supplemental information for other detail experiments.

CO oxidation

The catalytic activity of as–prepared metal oxides for CO oxidation was evaluated in a continuous–flow quartz reactor equipped with a straight quartz tube (diameter of 4 mm) at atmospheric pressure. The feed gas of 1% CO balanced with dry air passed through the catalyst bed at a flow rate of 10 mL min^{-1} (space velocity = 30 000 $mL{\cdot}gcat^{-1}{\cdot}h^{-1}$). The gas was controlled by mass flow controller (Horiba S49 32/MT), and the reaction temperature was adjusted from room temperature to the temperature of complete CO conversion. The CO concentration was analyzed by an on–line gas chromatograph (Buck Scientific 910) equipped with a dual molecular sieve/porous polymer column and a thermal conductivity detector. The CO conversion was calculated based on the content change of CO in feed gas and an effluent stream.

Oxygen evolution reaction

Electrochemical characterization was conducted on on a CHI604B electrochemical workstation in 1 M KOH with a rotating glassy carbon (GC) electrode as the working electrode, a Pt wire as the counter, and a Ag/AgCl as the reference. 5 mg of sample in 1 mL ethanol–water mixture (1:1) and 10 µl Nafion was thoroughly sonicated for 1 h. 10 µL of the catalyst ink was pipetted and spread onto the electrode, which was dried in air at room temperature. Pure oxygen gas was purged for 15 min before each OER test. The polarization curves were recorded at a scan rate of 5 mV s^{-1} and a rotation rate of 1600 rpm. Before collecting polarization curves, the working electrodes were scanned until the signals were stabilized. The overpotential η was calculated using the equation $\eta = E_{(vs.RHE)} - 1.23$, where $E_{(vs.\ RHE)}$ is the applied potential vs RHE

in 1 M KOH ($E_{RHE} = E_{Ag/AgCl} + 0.197 + 0.059\times pH$). The Tafel slope was calculated according to Tafel equation $\eta = b \times \log(\frac{j}{j_0})$.

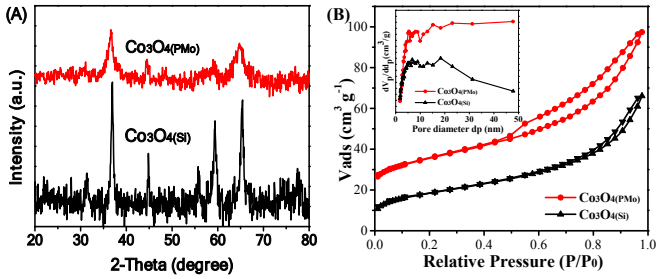

Figure 2. (A) XRD patterns and (B) N_2 adsorption–desorption isotherms of $Co_3O_{4(PMo)}$ and $Co_3O_{4(Si)}$. For clarity, the isotherm of $Co_3O_{4(PMo)}$ is offset along the y axis by 20 $cm^3\ g^{-1}$.

Results and discussion

Preparation and characterization of metal oxides

Mesoporous metal oxides were prepared through a mechanochemical process (**Figure 1**), which uses metal nitrate as precursor and POM as template. Typically, $Co(NO_3)_2$ was firstly mixed with $Na_3PMo_{12}O_{40}$ by ball milling for 30 min. During this process, the Co cations could be bonded with $PMo_{12}O_{40}^{3-}$ anions to form an ionic composite. Subsequent calcination of the mixture at 400 °C in air resulted in crystalline Co_3O_4 surrounding $PMo_{12}O_{40}^{3-}$ clusters, while the Keggin structure of $PMo_{12}O_{40}^{3-}$ was well retained as evidenced by characteristic XRD peaks for $PMo_{12}O_{40}^{3-}$ (**Figure S1**). Note that the decomposition temperature of $Na_3PMo_{12}O_{40}$ is higher than 450 °C, as demonstrated by TGA (**Figure S2**). After selective removal of $Na_3PMo_{12}O_{40}$, mesoporous Co_3O_4 was obtained (denoted as $Co_3O_{4(PMo)}$).

SEM images of $Co_3O_{4(PMo)}$ (**Figure S3**) present a bulk structure with apparent pores on the surface. The $Co_3O_{4(PMo)}$ sample is actually composed of irregular particle aggregations in nanoscale, who generate a high degree of interstitial porosity. Only Co and O signals were detected by EDS pattern, which indicates that $Na_3PMo_{12}O_{40}$ has been removed (Figure S2). FT–IR studies were carried out to analyze the skeletal structure of $Co_3O_{4(PMo)}$ (**Figure S4(A,B)**). The FT–IR spectrum of $Co_3O_{4(PMo)}$ before washing shows typical vibration peaks (559 and 656 cm^{-1}) for Co_3O_4 spinel phase and four characteristic peaks (1080, 970, 895, and 798 cm^{-1}) for the Keggin structure of $PMo_{12}O_{40}^{3-}$.[23,27] Four Keggin peaks disappeared after washing, indicating the removal of $Na_3PMo_{12}O_{40}$. Also, the FT–IR spectrum of the recovered $Na_3PMo_{12}O_{40}$ was very similar to that of the fresh one (**Figure S4C**), indicating an unchanged structure.

The XRD pattern of $Co_3O_{4(PMo)}$ in **Figure 2A** exhibits a group of diffraction peaks at 31.1°, 36.6°, 44.5°, 59.3° and 65.1°, which could be well–fitted with the responses of (111), (220), (311), (400), (511),

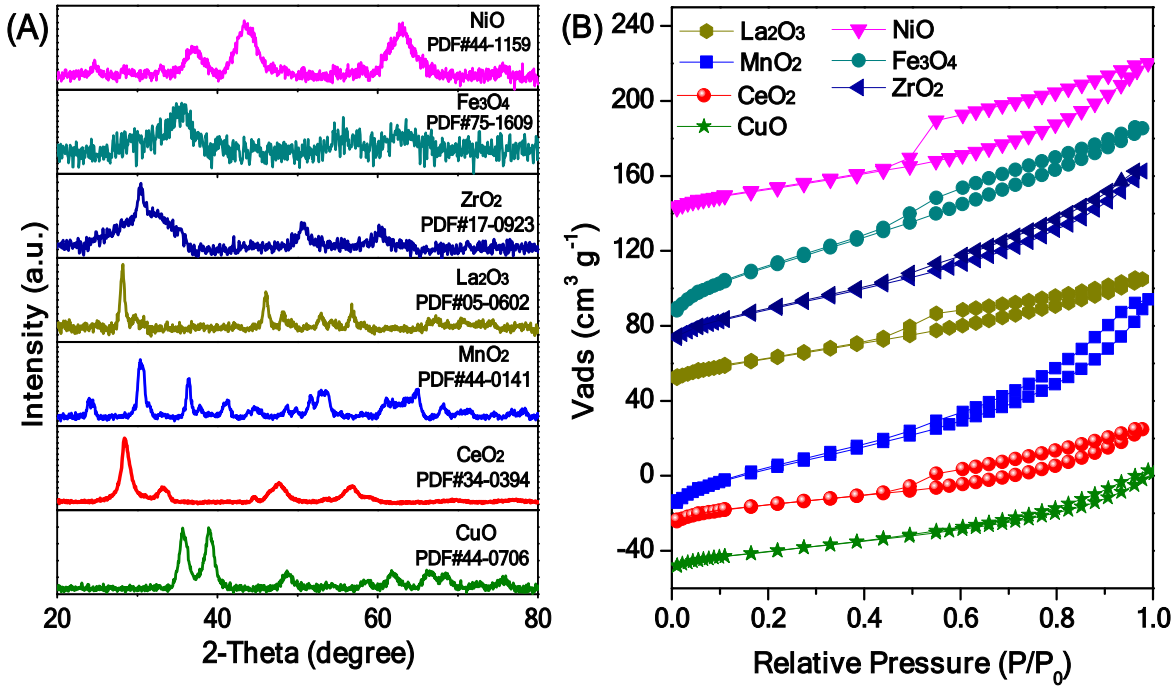

Figure 3. (A) XRD patterns and (B) N_2 adsorption–desorption isotherms of as-prepared metal oxides. For clarity, the isotherms of NiO, Fe_3O_4, ZrO_2, La_2O_3, CeO_2, and CuO are offset along the y axis by 140, 80, 50, -20, and -50 $cm^3\ g^{-1}$, respectively.

and (440) planes of cubic phase Co_3O_4, respectively. No XRD peaks assigned to $Na_3PMo_{12}O_{40}$ were detected. The Mo residues in Co_3O_4 were less than 0.5 wt% as determined by ICP-AES. These results further confirm the removal of $Na_3PMo_{12}O_{40}$. The relative broad and low diffraction peaks for $Co_3O_{4(PMo)}$ suggest the small crystallite size.

The porous structure of $Co_3O_{4(PMo)}$ was evaluated by N_2 sorption measurement at 77 K. As shown in **Figure 2B**, $Co_3O_{4(PMo)}$ exhibited a typical IV isotherm with a H3-type hysteresis loop between relative pressure P/P_0 = ~0.5–1.0, indicating the presence of mesopores. The specific surface area was estimated to be 168 m^2/g with an average pore size of 6.6 nm. By using $Na_3PW_{12}O_{40}$ instead of $Na_3PMo_{12}O_{40}$ as the template for fabrication of Co_3O_4, a similar mesoporous structure with specific surface area of 135 m^2/g was achieved (**Figure S5**). For comparison, a control Co_3O_4 sample (denoted as $Co_3O_{4(Si)}$) was prepared by using silica as the template. XRD pattern of $Co_3O_{4(Si)}$ also revealed a typical pure cubic phase of Co_3O_4 (Figure 2A). The relative strong peak intensity and narrow half peak width were probably due to larger crystallite size of $Co_3O_{4(Si)}$ compared with $Co_3O_{4(PMo)}$. The average particle size of $Co_3O_{4(Si)}$ was calculated by Scherrer's equation to be ~16 nm, which is larger than that of $Co_3O_{4(PMo)}$ (~5.5 nm) (**Table S1**). A low specific surface area of 93 m^2/g was obtained by $Co_3O_{4(Si)}$.

As large anion clusters, $PMo_{12}O_{40}^{3-}$ has strong ion pairing ability, which allows many metal cations to share one $PMo_{12}O_{40}^{3-}$ anion.[28] The XRD pattern for the ionic composite shows characteristic diffraction peaks for cobalt salt of POM (**Figure S6**).[28,29] Thus, the crystal structure of $PMo_{12}O_{40}^{3-}$ is supposed to be rearranged by introducing the Co cations, involving the assembly of cations and anions through electrostatic interactions. These features allow Co species recrystallize to Co_3O_4 around $PMo_{12}O_{40}^{3-}$ during the following pyrolysis, and rich pore channels were produced after the removal of $PMo_{12}O_{40}^{3-}$. It should be noted that a low mass ratio of $Na_3PMo_{12}O_{40}$ to metal precursor (1:1) could lead to a high surface area of 168 m^2/g for Co_3O_4, even a lower mass ratio of 0.5:1 can give rise to a surface area of 113 m^2/g (**Figure S7**). Moreover, due to the high thermal stability and preferred solubility, the structure of $Na_3PMo_{12}O_{40}$ maintained well during the whole preparation process for Co_3O_4, and the $Na_3PMo_{12}O_{40}$ can be recycled with a recovery rate of ~80 wt% by evaporation of water and reused. Using the recovered $Na_3PMo_{12}O_{40}$ as the temperature for preparation of Co_3O_4, a high specific surface of 128.6 m^2/g was achieved (**Figure S8**). Therefore, the current POM–templating mechanochemical method is facile, and probably scalable production of porous metal oxides.

To inquire the scope of POM–templating mechanochemical method, several metal oxides were prepared at 400 °C using different $M(NO_3)_x$ (M = Fe, Ni, Zr, La, Mn, Ce, Cu) as metal sources. The XRD patterns in **Figure 3A** reveal well crystalline structures for the corresponding oxides, and the diffraction peaks are in consistent with those of the JCPDS cards, respectively, confirming the success production of Fe_3O_4, NiO, ZrO_2, La_2O_3, MnO_2, CeO_2, and CuO. N_2 sorption studies (**Figure 3B**) show that all of these metal oxides exhibit type IV isotherms, indicating a mesoporous structure. Interestingly, Fe_3O_4 possesses a high specific surface area of 210 m^2/g. NiO (128 m^2/g), ZrO_2 (115 m^2/g), La_2O_3 (98 m^2/g), MnO_2 (177

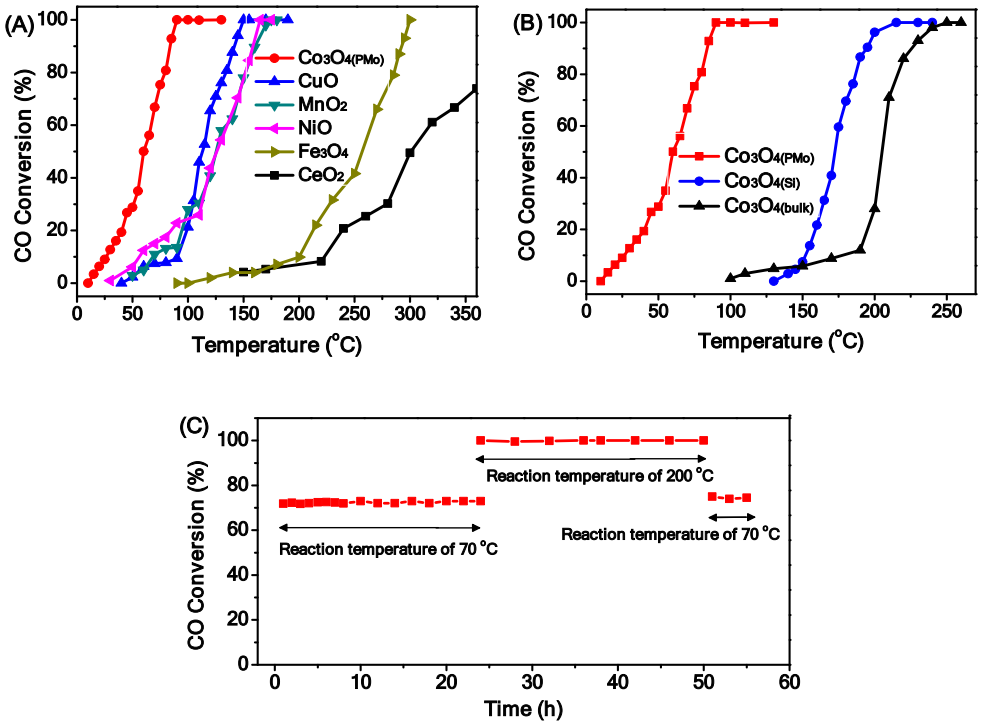

Figure 4. (A) CO oxidation over different mesoporous metal oxides; (B) CO oxidation over Co_3O_4–based samples; (C) The stability test of $Co_3O_{4(PMo)}$ in CO oxidation.

m^2/g), CeO_2 (112 m^2/g), and CuO (92 m^2/g) also display relative high surface areas. The values are higher or comparable to those reported in the previous literatures,[30-33] demonstrating a strong capability of the present strategy for the synthesis of a wide range of mesoporous metal oxides.

Catalytic test for CO oxidation

Metal oxides have been considered a substitute for precious metal catalysts for the oxidation of CO.[34-36] To demonstrate the possible improvements in catalytic performance with resulting porous metal oxides, the preferential CO oxidation was investigated in normal feed gas. As shown in **Figure 4**, $Co_3O_{4(PMo)}$ exhibited the best activity, 100% CO conversion was achieved at 90 °C (T_{100} = 90 °C). The T_{100} was lower than those of CuO (T_{100} = 150 °C), MnO_2 (T_{100} = 170 °C), NiO (T_{100} = 175 °C), Fe_3O_4 (T_{100} = 300 °C), and CeO_2 (T_{100} > 350 °C). In addition, the stability test for CO oxidation over $Co_3O_{4(PMo)}$ was performed at 70 °C and 200 °C, respectively (Figure 4C). A ~72% CO conversion can be achieved at 70 °C consecutively for 25 h. Subsequently, 100% CO conversion was maintained after running 25 h at 200 °C, and when the temperature was further decreased to 90°C, the CO conversion still maintained at 100%, demonstrating an excellent durability of $Co_3O_{4(PMo)}$. The catalytic performance of $Co_3O_{4(PMo)}$ is quite promising in terms of activity and stability when compared with the metal oxides (e.g. CoO, $CuCo_2O_4$, CuO_x, Co_3O_4-CeO_2) reported thus far,[37-40] and is even superior to some of supported noble metal catalysts.[41-43]

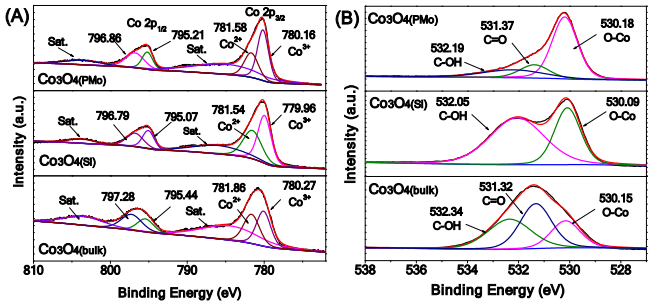

Figure 5. (A) Co 2p spectra and (B) O 1s spectra of $Co_3O_{4(PMo)}$, $Co_3O_{4(Si)}$, and $Co_3O_{4(bulk)}$.

Moreover, The $Co_3O_{4(PMo)}$ catalyst (T_{100} = 90 °C) is more active than $Co_3O_{4(Si)}$ derived from silica template (T_{100} = 200 °C) and commercial bulk Co_3O_4 (T_{100} = 250 °C). (Figure 4B). This indicates that the mesopore and large surface area are intrinsically favorable for CO oxidation in the aspect of active site exposure and reactant access. However, the porosity does not seem to cause such strong influence on the catalyst performance, because both $Co_3O_{4(PMo)}$ and $Co_3O_{4(Si)}$ have high specific surface areas of 168 m^2/g and 93 m^2/g, respectively. Therefore, there might be other factors responsible for the activity differences.

To gain further insight into the correlation between catalyst structure and activity in CO oxidation, $Co_3O_{4(PMo)}$ and control Co_3O_4 samples were characterized by XPS analysis. In the Co 2p XPS spectra of three Co_3O_4 samples (**Figure 5A**), the signals at ~780 eV

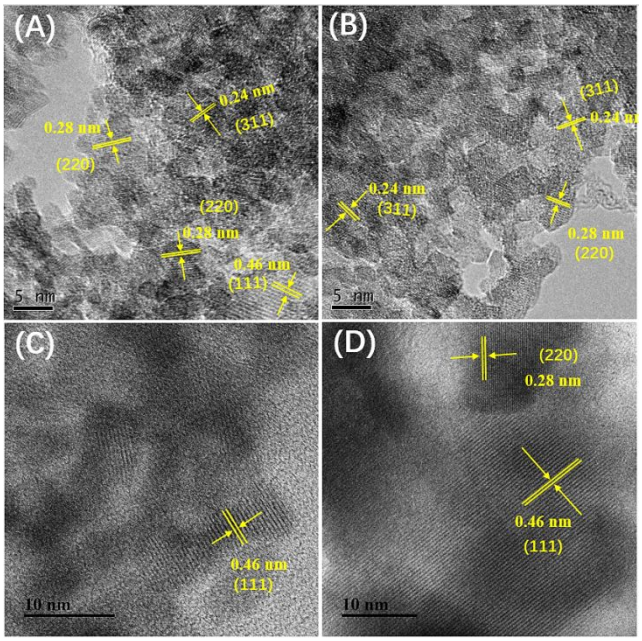

Figure 6. HRTEM images of (A and B) $Co_3O_{4(PMo)}$, (C) $Co_3O_{4(Si)}$, and (D) $Co_3O_{4(bulk)}$.

and ~795 eV were assigned to the surface Co^{3+} species and the signals at ~781 eV and ~797 eV to surface Co^{2+} species, whereas the low intensity broad peaks that appeared at ~787 and ~804 eV were characteristic shake-up satellites of Co_3O_4.[44] The atomic ratio of Co^{3+}/Co^{2+} on the surface of Co_3O_4 samples was calculated based on the area of XPS fitting results. The Co^{3+}/Co^{2+} ratio decreased according to the sequence of $Co_3O_{4(PMo)}$ (1.66) > $Co_3O_{4(Si)}$ (1.16) > $Co_3O_{4(bulk)}$ (1.07) (**Table S1**). The peaks at binding energy ~535–528 eV were characteristic of O 1s, which can be resolved into the surface lattice oxygen O_{latt} (~530 eV) and adsorbed oxygen (O_{ads}, e.g., O^{2-}, O_2^{2-} or O^-) (531–533 eV), respectively (**Figure 5B**).[45-47] Obviously, $Co_3O_{4(PMo)}$ possessed a high O_{latt}/O_{ads} ratio (1.812) than those of $Co_3O_{4(Si)}$ (0.578) and $Co_3O_{4(bulk)}$ (0.292) (Table S1). The existence of a higher amount of oxygen lattices should be associated with a surface enrichment effect of Co^{3+} species for $Co_3O_{4(PMo)}$. The XPS result clearly indicates that the template played an important role in determining the surface elemental composition of Co_3O_4.

HRTEM images were took to identify the exposed planes of three Co_3O_4 samples. Only the normal (111) plane with a lattice spacing of 0.46 nm was observed for both $Co_3O_{4(Si)}$ and $Co_3O_{4(bulk)}$ (**Figure 6C and 6D**), suggesting that the {001} facets dominate the surface. The HRTEM images of $Co_3O_{4(PMo)}$ show a wormhole–like structure with rich porous channels (**Figure 6A and 6B**). The lattice fringes of 0.28 nm, 0.24, and 0.46 nm, corresponding to the (220), (311), and (111) planes of the cubic Co_3O_4 spinel structure could be observed, respectively, which means that abundant {110} facets were exposed on the surface of $Co_3O_{4(PMo)}$. It has been proved that Co^{3+} cations are present solely on the {110} plane, while {001} plane contains only Co^{2+} cations.[48-50] HRTEM observation further evidences that

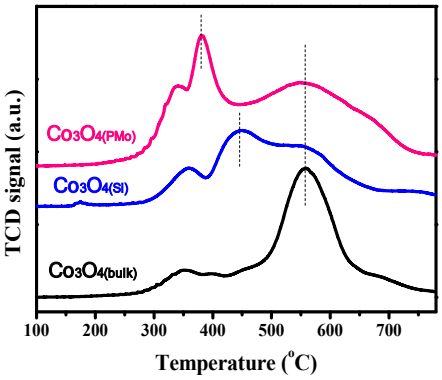

Figure 7. H_2–TPR profiles of $Co_3O_{4(PMo)}$, $Co_3O_{4(Si)}$, and $Co_3O_{4(bulk)}$.

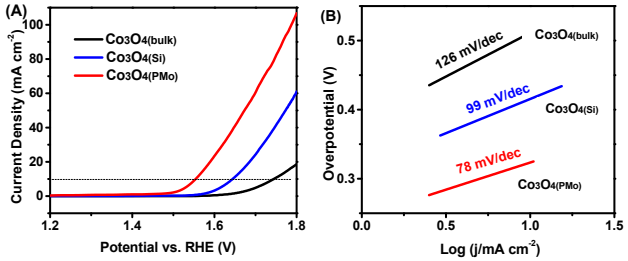

Figure 8. (A) LSV curves and (B) corresponding Tafel plots of $Co_3O_{4(PMo)}$, $Co_3O_{4(Si)}$, and $Co_3O_{4(bulk)}$ for OER in 1 M KOH.

$Co_3O_{4(PMo)}$ is rich in Co^{3+} active sites, in agreement with the XPS results.

The high content of Co^{3+} species for $Co_3O_{4(PMo)}$ is suggested to arise from the ion pairing ability, as well as the strong redox capacity of POM.[28,51] The ionic bonding between Co cations and $PMo_{12}O_{40}^{3-}$ anion makes the Co_3O_4 crystal grow along the surface of bulky $PMo_{12}O_{40}^{3-}$ cluster. As this process was performed in air at a high temperature of 400 °C, $PMo_{12}O_{40}^{3-}$ becomes a powerful oxidant for Co species. The Co^{2+} species at the interface with $PMo_{12}O_{40}^{3-}$ cluster can be oxidized to Co^{3+}, and thus more Co^{3+} species are exposed after the removal of $PMo_{12}O_{40}^{3-}$. Co^{3+} species in Co_3O_4 are well known active sites for CO oxidation.[48-50] The higher amount of exposed Co^{3+} sites makes the CO oxidation more favorable in $Co_3O_{4(PMo)}$.

The redox properties of $Co_3O_{4(PMo)}$, $Co_3O_{4(Si)}$, and commercial $Co_3O_{4(bulk)}$ were investigated by temperature–programmed reduction with hydrogen (H_2–TPR) (**Figure 7**). In the profile of $Co_3O_{4(PMo)}$, the shoulder reduction peak at 320 °C could be ascribed to the desorption of surface-active oxygen species such as O^{2-} and O^-, the second peak at 360 °C was assigned to the reduction of Co^{3+} to Co^{2+}, and the broad peak from 500 to 700 °C was attributed to the reduction of Co^{2+} to Co^0.[52-54] In the case of $Co_3O_{4(Si)}$, a higher reduction temperature of ~420 °C for $Co^{3+}\rightarrow Co^{2+}$ was required. Commercial $Co_3O_{4(bulk)}$ gave a broad peak at 550 °C, which can be assigned to the direct reduction of Co^{3+} to Co^0.[52] This observation trend is in consistent with the previous reports that Co_3O_4 of large particles often possess a single step via $Co^{3+}\rightarrow Co^0$, while Co_3O_4 of nanoparticles usually undergo a two-step process of $Co^{3+}\rightarrow Co^{2+}\rightarrow Co^0$ with a faster reduction rate.[46,53,54] It is widely acknowledged that the lower reduction temperature for $Co^{3+}\rightarrow Co^{2+}$ in Co_3O_4 makes oxidation more favorable. Therefore, the best low–temperature reducibility of $Co_3O_{4(PMo)}$ for $Co^{3+}\rightarrow Co^{2+}$ was another factor influencing its catalytic performance in CO oxidation.

Catalytic test for OER

We furhter compared the OER activity of $Co_3O_{4(PMo)}$ with $Co_3O_{4(Si)}$ and $Co_3O_{4(bulk)}$ in 1 M KOH using a three electrode system. **Figure 8A** illustrates the linear sweep voltammetry (LSV) cures of these samples. To achieve a current density of 10 mA cm^{-2}, $Co_3O_{4(bulk)}$ displayed a very high onset overpotential of 514 mV, whereas Co@NC showed an overpotential of 414 mV. Remarkably, $Co_3O_{4(PMo)}$ exhibited significantly enhanced electrocatalytic activity, a low overpotential of 254 mV was achieved at a current density of 10 mA cm^{-2}. The Tafel slope of the three samples were calculated from the LSV curves (**Figure 8B**). $Co_3O_{4(PMo)}$ showed the smallest Tafel slope of 78 mV/dec among the values of 99 mV/dec for $Co_3O_{4(Si)}$ and 126 mV/dec for bulk $Co_3O_{4(bulk)}$, suggesting better kinetics and superior electro–activity. For the durability of $Co_3O_{4(PMo)}$, the LSV curves exhibited almost no activity loss before and after 1000 continuous potential cycling at an accelerated scanning rate of 100 mV s^{-1} (**Figure S9**), suggesting excellent stability of $Co_3O_{4(PMo)}$ for OER. These results further confirm that the present POM–templating mechanochemical synthesis strategy for metal oxides allows improvement of the catalytic performance.

Conclusions

By combination of good thermal stability, preferred solubility in water, strong ion pairing ability, and oxidative capacity, POM is actually an inherent template, yet has not been explored before. In this study, a facile, rapid and general mechanochemical strategy, using Keggin type POM as template and metallic nitrate as precursor, was introduced for the synthesis of a series of mesoporous metal oxides (Co_3O_4, Fe_3O_4, NiO, La_2O_3, MnO_2, CeO_2, ZrO_2, and CuO) with high specific surface areas (up to 210 m^2g^{-1}). POM, as a recyclable bifunctional template, could incorporate both abundant porosity and reactive surfaces into metal oxides. Interestingly, mesoporous $Co_3O_{4(PMo)}$ (T_{100}=90°C) with enriched Co^{3+} cations on the surface was found to be more active than $Co_3O_{4(Si)}$ (T_{100}=200°C) and commercial $Co_3O_{4(Bulk)}$ (T_{100}=250°C) in CO oxidation. The same catalytic trend was also observed in the oxygen evolution reaction. The present methodology of synthesizing mesoporous metal oxides with controllable surface is highly attractive, which may be extended to the design of task-specific metal oxides for catalysis.

Acknowledgements

The authors thank the National Natural Science Foundation of China (no. 21978115). S. D. and H. C. were supported by the Division of Chemical Sciences, Geosciences and Biosciences, Office of Basic

Energy Sciences, U.S. Department of Energy. Y. L. was supported by the central laboratory of the School of Chemical and Material Engineering. P. F. Z. acknowledges the Thousand Talents Program, National Natural Science Foundation of China (Grant No. 21776174), the Open Foundation of the State Key Laboratory of Ocean Engineering (Shanghai Jiao Tong University of China) (No. 1809), and the China Shipbuilding Industry Corporation for their support.

Notes

The authors declare no competing financial interest.

References

1 Y. Zhao, L. P. Wang, M. T. Sougrati, Z. Feng, Y. Leconte, A. Fisher, M. Srinivasan, Z. Xu, *Adv. Energy Mater.,* 2017, *7*, 1601424.
2 G. S. Hutchings, Y. Zhang, J. Li, B. T. Yonemoto, X. Zhou, K. Zhu, F. Jiao, *J. Am. Chem. Soc.,* 2015, *137*, 4223–4229.
3 B. Dutta, S. March, L. Achola, S. Sahoo, J. He, A. S. Amin, Y. Wu, S. Poges, S. P. Alpay, S. L. Suib, *Green Chem.,* 2018, *20*, 3180–3185.
4 H. Wang, S. Zhuo, Y. Liang, X. Han, B. Zhang, *Angew. Chem. Int. Ed*. 2016, *55*, 9055–9059.
5 J. Fang, L. Zhang, J. Li, L. Lu, C. Ma, S. Cheng, Z. Li, Q. Xiong, H. You, *Nature Commun*., 2018, *9*, 521.
6 Y. Ren, Z. Ma, P. G. Bruce, *Chem. Soc. Rev*. 2012, *41*, 4909–4927.
7 J. Byun, H. A. Patel, D. J. Kim, C. H. Jung, J. Y. Park, J. W. Choi, C. T. Yavuz, *J. Mater. Chem. A*, 2015, *3*, 15489-15497.
8 Q. Zhang, J. Wang, J. Dong, F. Ding, X. Li, B. Zhang, S. Yang, K. Zhang, *Nano Energy,* 2015, *13*, 77–91.
9 Q. Zhu, Q. Xu, *Chem*., 2016, *1*, 220-245.
10 D. Luo, B. Chen, X. Li, Z. Liu, X. Liu, X. Liu, C. Shi, X. S. Zhao, *J. Mater. Chem. A*., 2018. *6*, 7897–7902.
11 Y. Wang, H. Arandiyan, J. Scott, A. Bagheri, H. Dai, R. Amal, *J. Mater. Chem. A,* 2017, *5*, 8825–8846.
12 S. Tanaka, Y. V. Kaneti, R. Bhattacharjee, M. N. Islam, R. Nakahata, N. Abdullah, S. Yusa, N. T. Nguyen, M. J. A. Shiddiky, Y. Yamauchi, M. S. A. Hossain, *ACS Appl. Mater. Interfaces*, 2018, *10*, 1039–1049.
13 J. Feng, Y. Yin, *Adv. Mater*., 2018, 30, 1802349.
14 Y. Wang, H. Arandiyan, J. Scott, A. Bagheri, H. Dai, R. Amal, *J. Mater. Chem. A,* 2017, *5*, 8825–8846.
15 S. Tanaka, Y. V. Kaneti, R. Bhattacharjee, M. N. Islam, R. Nakahata, N. Abdullah, S. Yusa, N. T. Nguyen, M. J. A. Shiddiky, Y. Yamauchi, M. S. A. Hossain, *ACS Appl. Mater. Interfaces*, 2018, *10*, 1039–1049.
16 V. Malgras, H. Ataee-Esfahani, H. Wang, B. Jiang, C. Li, K. C. W. Wu, J. H. Kim, Y. Yamauchi, *Adv. Mater*. 2016, *28*, 993–1010.
17 J. Yang, T. Zhou, R. Zhu, X. Chen, Z. Guo, J. Fan, H. K. Liu, W. X. Zhang, *Adv. Mater. Interfaces,* 2016, *3*, 1500464.
18 N. Yang, F. Pang, J. Ge, *J. Mater. Chem. A*, 2015, *3*, 1133–1141.
19 Y. Ren, Z. Ma, L. Qian, S. Dai, H. He, P. G. Bruce, *Catal. Lett.* 2009, *131*,146–154.
20 W. Xiao, S. Yang, P. Zhang, P. Li, P. Wu, M. Li, N. Chen, K. Jie, C. Huang, N. Zhang, S. Dai, *Chem. Mater*., 2018, *30*, 2924−2929.
21 X. Deng, K. Chen, H. Tuysuz, *Chem. Mater*. 2017, *29*, 40−52.
22 L. Shang, R. Shi, G. I. N. Waterhouse, L. Z. Wu, C. H. Tung, Y. Yin, T. Zhang, *Small Methods*, 2018, *2*, 1800105.
23 K. Wang, Y. Cao, J. Hu, Y. Li, J. Xie, D. Jia, *ACS Appl. Mater. Interfaces,* 2017, *9*, 16128−16137.
24 S. Omwoma, C. T. Gore, Y. Ji, C. Hu, Y. F. Song, Coordin. Chem. Rev., 2015, *286*, 17−29.
25 S. Wang, G. Yang, *Chem. Rev.,* 2015, *115*, 4893–4962.
26 T. Boyd, S. G. Mitchell, D. Gabb, D. L. Long, Y. F. Song, L. Cronin, *J. Am. Chem. Soc.,* 2017, *139*, 5930–5938.
27 Y. Leng, J. Li, C. Zhang, P. Jiang, Y. Li, S. Du, J. Mater. Chem. A, 2017, *5*, 17580−17588.
28 W. Luo, J. Hu, H. Diao, B. Schwarz, C. Streb, Y. F. Song, *Angew. Chem. Int. Ed*., 2017, *56*, 4941–4944.
29 S. Benadji, T. Mazari, L. Dermeche, N. Salhi, E. Cadot, C. Rabia, *Catal. Lett.* 2013, *143*, 749-755.
30 C. H. Kuo, I. M. Mosa, A. S. Poyraz, S. Biswas, A. M. El-Sawy, W. Song, Z. Luo, S. Chen, J. F. Rusling, J. He, S. L. Suib, *ACS Catal*., 2015, *5*, 1693−1699.
31 R. R. Salunkhe, Y. V. Kaneti, Y. Yamauchi, *ACS Nano*. 2017, *11*, 5293−5308.
32 B. M. Mogudi, P. Ncube, R. Meijboom, *Applied Catalysis B: Environmental,* 2016, *198*, 74−82.
33 Y. Zheng, W. Wang, D. Jiang, L. Zhang, X. Li, Z. Wang, *J. Mater. Chem. A*, 2016, **4**, 105−112.
34 J. Jansson, *J. Catal.*, 2000, *194*, 55−60.
35 C. J. Jia, M. Schwickardi, C. Weidenthaler, W. Schmidt, S. Korhonen, B. M. Weckhuysen, F. Schüth, *J. Am. Chem. Soc.,* 2011, *133*, 11279–11288.
36 F. Teng, M. Chen, G. Li, Yang Teng, T. Xu, Y. Hang, W. Yao, S. Santhanagopalane, D. D. Menge, Y. Zhu, *Appl. Catal. B: Environ.,* 2011, *110*, 133–140.
37 D. Gu, C. Jia, C. Weidenthaler, H. Bongard, B. Spliethoff, W. Schmidt, F. Schüth, *J. Am. Chem. Soc*., 2015, *137*, 11407−11418.
38 W. Wang, P. Du, S. Zou, H. He, R. Wang, Z. Jin, S. Shi, Y. Huang, R. Si, Q. Song, C. Jia, C. Yan, *ACS Catal.* 2015, *5*, 2088-2099.
39 W. Tang, M. Yao, Y. Deng, X. Li, N. Han, X. Wu, Y. Chen, *Chem. Eng. J.*, 2016, *306*, 709–718.
40 J. Q. He, D. Y. Chen, N. J. Li, Q. F. Xu, H. Li, J. H. He, J. M. Lu, *ChemSusChem*, 2019, *12*, 1084-1090.
41 Z. Zhang, Y. Zhu, H. Asakura, B. Zhang, J. Zhang, M. Zhou, Y. Han, T. Tanaka, A. Wang, T. Zhang, N. Yan, *Nature Commun.*, 2017, 16100.
42 X. Zhang, H. Dong, Y. Wang, N. Liu, Y. Zuo, L. Cui, *Chem. Eng. J.*, 2016, *283*, 1097–1107.
43 H. Zhu, Z. Wu, D. Su, G. M. Veith, H. Lu, P. Zhang, S. Chai, S. Dai, *J. Am. Chem. Soc*., 2015, *137*, 10156−10159.
44 L. Lukashuk, K. Föttinger, E. Kolar, C. Rameshan, D. Teschner, M. Hävecker, A. Knop-Gericke, N. Yigit, H. Li, E. McDermott, M. Stöger-Pollach, G. Rupprechter, *J. Catal.*, 2016, *344*, 1–15.
45 Y. Lou, J. Ma, X. Cao, L. Wang, Q. Dai, Z. Zhao, Y. Cai, W. Zhan, Y. Guo, P. Hu, G. Lu, Y. Guo, *ACS Catal*., 2014, *4*, 4143–4152.
46 J. González-Prior, R. López-Fonseca, J. I. Gutiérrez-Ortiz, B. de Rivas, *Appl. Catal. B: Environ.*, 2018, *222*, 9–17.
47 Y. Du, Q. Meng, J. Wang, J. Yan, H. Fan, Y. Liu, H. Dai, Micropor. Mesopor. Mater., 2012, 162, 199-206.
48 X. Xie, Y. Li, Z. Q. Liu, M. Haruta, W. Shen, *Nature*, 2009, *458*, 746–749.
49 C. Y. Ma, Z. Mu, J. J. Li, Y. G. Jin, J. Cheng, G. Q. Lu, Z. P. Hao, S. Z. Qiao, *J. Am. Chem. Soc*., 2010, *132*, 2608–2613.
50 J. Ding, L. Li, H. Zheng, Y. Zuo, X. Wang, H. Li, S. Chen, D. Zhang, X. Xu, G. Li, *ACS Appl. Mater. Interfaces*., 2019**,** *11*, 6042–6053.
51 Y. Wang, I. A. Weinstock, *Chem. Soc. Rev*., 2012, *41*, 7479–7496.
52 Q. Wang, Y. Peng, J. Fu, G. Z. Kyzas, S. M. R. Billah, S. An, *Appl. Catal. B: Environ*., 2015, *168–169*, 42–50.

53 Y. Lou, L. Wang, Z. Zhao, Y. Zhang, Z. Zhang, G. Lu, Y. Guo, Y. Guo, *Appl. Catal. B: Environ.*, 2014, *146*, 43–49.
54 Z. Wu, J. Deng, Y. Liu, S. Xie, Y. Jiang, X. Zhao, J. Yang, H. Arandiyan, G. Guo, H. Dai, *J. Catal.,* 2015*, 332*, 13–24.